Theoretical Calculation of High-Pressure CO_2 Jet under Composite Rock-Breaking Based on Span-Wagner State Equation

Xian-Peng Yang[1,3], Can Cai[1,2,3,4*], Xiao-Hua Chen[5], Pei Zhang[1,3], Xin Zeng[1,3], Chi Peng[3,4], Ying-Fang Zhou[2]

1. Oil and gas equipment technology Sharing and Service Platform of Sichuan Province, School of Mechanical Engineering, Southwest Petroleum University, Chengdu 610500, P.R. China;
2. School of Engineering, University of Aberdeen, Aberdeen, AB24 3FX, United Kingdom;
3. Laboratory of High-pressure Jet Theory and Application Technology, Southwest Petroleum University, Chengdu 610599, P.R. China;
4. Key Laboratory of Groundwater Resources and Environment (Jilin University), Ministry of Education, Changchun 130021, P.R. China;
5. Southwest Pipeline Co., Ltd., National Pipe Network Group, Chengdu, 610064, P.R. China;
*Corresponding author: School of Mechanical Engineering, Southwest Petroleum University, Chengdu, 610500, China. / School of Engineering, University of Aberdeen, Aberdeen, AB24 3FX, United Kingdom;
Email address: cainiao10@163.com / can.cai@abdn.ac.uk (C. Cai).
ORCID: 0000-0002-6762-9968 (Can Cai)

Abstract: Although some theoretical calculation methods for high-pressure jet have been proposed, there is currently no theoretical model for high-pressure CO_2 jet based on high-precision state equation. Aim to investigate the flow field of high-pressure CO_2 jet under high-pressure CO_2 Jet & PDC cutter composite rock-breaking, a semi-analytical approach of high-pressure CO_2 jet flow field was established based on the Span-Wagner state equation and CO_2 jet theory. Semi-analytical calculations and physical properties calculations with the high-pressure CO_2 jet were conducted considering the factors of jet pressure, jet distance, nozzle diameter and jet angle. The results indicate that the physical properties distribution calculated by the semi-analytical approaches is similar to that of experiment and numerical simulation, which indicates that the calculation method of high-pressure CO_2 jet presented in the study is effective and reliable. CO_2 jet obtained by theoretical calculation has obvious divergence characteristics, the density difference can reach 800 Kg/m^3 between the initial region and the jet impact region. At the temperature of 300K, the increase in initial pressure can effectively increase the impact force and the cooling ability of the jet. The increase in the ratio of nozzle diameter and jet length can increase the proportion of the jet core lengths in the jet on the axis, which can enhance the impact force of the jet. The increase in the jet angle can increase the impact force of the fluid, but it is not conducive to fluid diffusion. The study combines the theoretical calculation of jet with the physical properties calculation of high-pressure CO_2 firstly, comprehensively understanding the CO_2 jet field in the composite rock-breaking of high-pressure CO_2 jet & PDC cutter. The study has a promoting effect on the theoretical calculation of CO_2 jet based on the high-precision state equation, and has great significance for the convenient calculation of CO_2 drilling in practical engineering.

Key Words: High-Pressure CO_2 jet; Impinge jet; Theoretical calculation; State equation; Physical property;

0 Introduction

With the decrease of shallow geological resources, deep geological resources have gradually become the focus of exploration and development in various countries. In the known deep geological resources, geothermal resources and deep oil-gas resources show superior exploitation value and exploitation potential, which are one of the main directions of energy development. However, there are widespread problems like high temperature, high pressure, complex geological environment and high rock strength in the drilling and completion of deep resources. This leads to serious problems, such as low rate of penetrate (ROP), severe thermal wear and severe bit loss during the drilling process, which brings great obstacles to the exploitation of deep resources.

High-pressure carbon dioxide (CO_2) is regarded as an alternative solution for the above problems because it can improve oil-gas production, reduce drilling difficulties and reduce environmental pollution [1]. The rock-breaking performance of high-pressure CO_2 jet is significantly improved over the high-pressure water jet, and there is an optimal nozzle diameter and jet distance to make the rock-breaking ability strongest [2]. Under the same working conditions, the CO_2 jet can always provide better rock-breaking performance than the water jet [3]. The intense rock-breaking ability of high-pressure CO_2 jet is mainly attributes to the impact pressure of the jet, and the other reason is the energizing effect caused by the phase transition from liquid to gas, leading to more debris [4].

High-pressure CO_2 jet could effectively promote the decomposition of clay minerals, change the micro-structure of shale, and permeate into rock [5]. In addition, high-pressure CO_2 jet also has the potential for enhancing heat transfer, so it has a stronger cooling effect than water [6], and it has a stronger cooling area that N_2 [7]. For the well completion, CO_2 fracturing technology is one of the main completion technologies at present. The purpose of fracturing is to improve the gas permeability of a stratum by the high-pressure injection of fracturing fluid into cracks [8,9]. Pulse high-pressure CO_2 jet fracturing creates more complex fracture morphology, larger fracture volume and CO_2 absorption than that of pulse water jet fracturing. Drilling technology is the premise of well completion technology, and high-pressure CO_2-assisted drill bit rock-breaking is one of the main development trends at present. The rock-breaking threshold pressure of supercritical CO_2 jet is higher than that of water jet [2]. Therefore, according to the unique performance of permeability, heat transfer, and rock-breaking mechanic, it is would be an effective way to exploit geothermal and deep oil-gas resources by using the high-pressure CO_2 jet assisting drill bit [10].

When the pressure is larger than the critical pressure, CO_2 exists in the liquid state, when the temperature is also larger than the critical temperature, CO_2 will be transformed into the supercritical fluid. In the field of oil & gas development, supercritical CO_2 jet fracturing technology has been widely studied and applied [11,12]. However, in the field of geothermal energy and deep oil & gas, the research and application of high-pressure CO_2 jet have not been fully developed, and the advantages of high-pressure CO_2 jet have not been fully applied. The main advantage of high-pressure CO2 jets in drilling is their stronger rock-breaking ability than other drilling fluids. High-pressure CO_2 has many outstanding properties such as high density similar to liquid, low viscosity and high diffusivity similar to gas, which makes high-pressure CO_2 jet has unique advantages in rock breaking and drilling [13]. High-pressure CO_2 jet has obvious oscillation impacting properties, the high rock-breaking efficiency of it is due to its self-exited oscillation impacting properties, it can cause larger mass losses than the continuous jets [14]. The rock breaking threshold pressure of high-pressure CO_2 jet in granite is only two-thirds of that of water jet, and less than half in sandstone [2]. Under the impact of high-pressure CO_2 jet, the compressive strength of rock decreases obviously, and core permeability is larger than water. Under the same experimental conditions, the rock breaking depth of high-pressure CO_2 jet is 1.65-1.85 times that of water jet [3]. In addition, under the condition of the same injection distance, the temperature difference of CO_2 jet is much larger than that of water jet and nitrogen jet, and the large temperature difference is also the main contribution for rock breakage [15].

Despite all the above advantages, the characteristics and structure of the flow field of high-pressure CO_2 jet fluid in the bottom are still unknown, and the interaction mechanism between the jet and rock is still unclear. Most studies pay more attention to the results of jet action on rock, but ignore the study of jet structure and distribution law of jet fluid. During the spraying, jet structure and its distribution characteristics of physical properties have some significant affect basic properties of the jet, such as impact force, flow velocity and fluid temperature, so it also has a great influence on the rock-breaking ability of the jet. To study this effect, a series of studies were carried out in the early stage. In 1994, Miller [16] started the research on the theory of high-pressure CO_2 jet and the two-phase flow. The research results show that during the downstream wall jet process of the high-pressure CO_2 jet, a thin-walled layer will be formed on the wall, which makes the fluid and solid particles move faster. Khali [17] conducted experiments and numerical calculations of high-pressure CO_2 jets, and the results indicated that at high pressures, CO_2 jet will produce violent phase transitions and expansions, and condensation will occur during the expansion. The research of Cheng et al. [18] shows that during the jet impacting the wall, the fluid velocity decreased and the pressure increased, and the maximum impact pressure generated by the CO_2 jet impact was larger than that of the water jet. The numerical simulation results of Zhou et al. [19] indicated that the CO_2 jet flow field can be divided into five areas according to flow characteristics. It was found through experiments of Huang et al. [20] that the potential core of the high-pressure CO_2 jet showed a length of about 9d and a small increasing trend with the increase of the inlet pressure. In addition, Cai et al. [11] observed the process of CO_2 jets and found that high-pressure CO_2 jet develops to fully jetting in only 0.07s, and a strong mixing exists in the annular region between the

96   jet core and the surroundings.

97   Although current studies proposed some theoretical calculation methods for high-pressure jet, but there is
98   currently no theoretical model and calculation method for high-pressure CO_2 jet based on high-precision state
99   equation. And the specific interaction mechanism between jet and PDC cutter is still not clear. Based on the previous
100   research [10,21], this paper established a semi-analytical approach of flow fluid under high-pressure CO_2 jet & PDC
101   cutter composite rock-breaking. In the semi-analytical approaches, the physical properties distribution of high-
102   pressure CO_2 jet was obtained by theoretical calculation equation of jet structure and Span-Wagner state equation.
103   The accuracy of the semi-analytical approach results was verified by comparison with experimental results and
104   numerical results. The influence law was obtained by comparative studies of jet with different jet distance, jet
105   pressure, jet angle and nozzle diameter, and its internal mechanism was analyzed. The findings of this research
106   combined the theoretical calculation of jet with the physical properties' calculation of CO_2, and provide a deep
107   understanding of the high-pressure CO_2 jet structure. This research has a promoting effect on the theoretical
108   calculation of CO_2 jet based on the high-precision state equation, and has great significance for the convenient
109   calculation of CO_2 drilling in practical engineering.

1 Calculation Model of High-Pressure CO_2 Impinge Jet

1.1 Physical Model

112   The experiment model (Fig. 1(a)) was established according to the real buttonhole model of the composite
113   high-pressure CO_2 jet and PDC cutter. In the process of drill bit drilling, the composite jet and PDC cutter together
114   work as one functional unit in the drill bit. The PDC cutting direction, jet injection direction and nozzle inclination
115   angle in the experimental model were designed according to the drill bit structure. The nozzle of the high-pressure
116   CO_2 jet was arranged at the height 15 mm above the cutter. The outlet of the nozzle faces the cutting edge with an
117   inclination angle of 45°. The cutters moved synchronously with the nozzle and the depth of the cutters was 2 mm,
118   the convergence angle of jet nozzle was 13.5° and the length of the stable section of the cylinder was two times of
119   the diameter of the nozzle. The schematic diagram was obtained by abstracting the basic function unit, as is shown
120   in Fig. 1(b).

121   During the composite rock-breaking of high-pressure CO_2 & PDC cutter, the CO_2 jet shows a large number of
122   advantages of debris carrying, heat transferring and cutting load reduction [2,10,21]. These advantages are mainly
123   own to the fluid phase change and gas expansion of CO_2 after jetting into wellbore. According to the previous
124   studies, even the flow field of CO_2 jet was observed by camera, there is absent of physical model to describe the
125   jetting flow at the region between cutter and nozzle. Therefore, the first essential aim of this study is aim to
126   established the physical model of the high-pressure CO_2 oblique jet between the cutter and the nozzle.

(a) Experiment model   (b) Schematic diagram
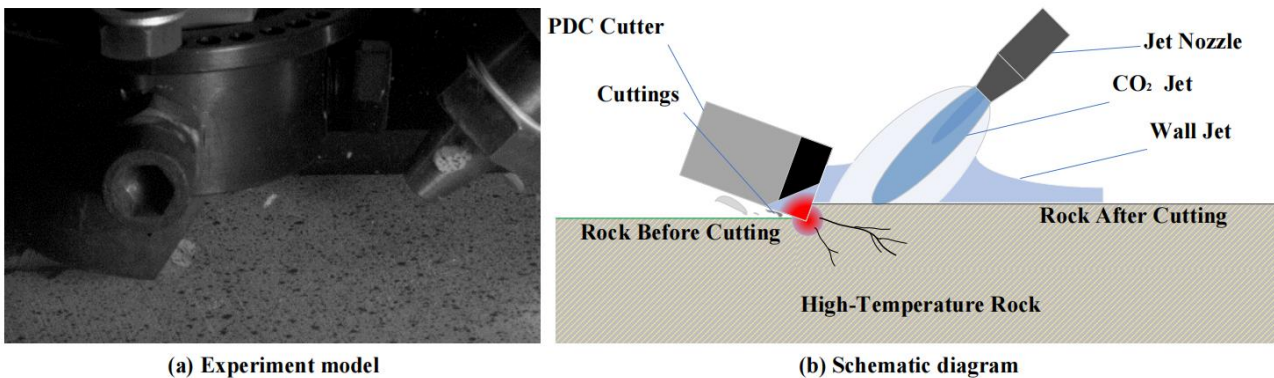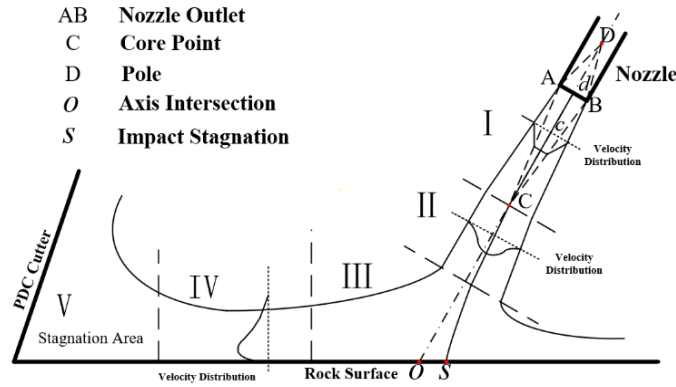
Fig. 1 Physical model of high-pressure CO_2 jet in composite work

129   Based on jet mechanics [22,23], and combined with the actual wellbore conditions of high-pressure CO_2 jet &
130   PDC cutter, the jet structure model of high-pressure CO_2 jet & PDC cutter was firstly proposed and established in
131   this paper, as is shown in Fig. 2. According to the gas jet structure, the jet was divided into five regions:

132   I. Initial region of free jet;

133   II. Development region of free jet;

134   III. Jet impact region;

135   IV. Wall jet region;

136   V. Impact stagnation region.

137   In the initial region of the free jet, the jet retains the core uniform velocity field in the development process, as

138   shown in the triangle *ABC* in Fig. 2. In the development region of the free jet, the jet velocity continues to decline.

139   In the jet impact region, the dynamic pressure of the CO_2 jet changes to static pressure with a giant pressure gradient.

140   The maximum impact pressure *Ps* will be generated at the impact stagnation point *S*. In the wall jet region, the fluid

141   is driven by the giant pressure gradient in the impact region and flows along the wall. Then, the Impinge jet gradually

142   evolves into the wall jet. When the wall jet impacts the PDC cutter surface, a stagnation zone generates in front of

143   the cutter.

144   The theoretical model in this research is two-dimensional, so the three-dimensional divergence of the high-

145   pressure CO_2 jet and the fluid loss on the side of the PDC cutter are not considered. Based on these simplifications,

146   theoretical calculations of flow field and physical properties of the composite CO_2 jet and PDC cutter are carried

147   out.

148

149   Fig. 2 Structural model of high-pressure CO_2 jet in cooperative work ()

150   *1.2 Theoretical Calculation*

151   According to the partition theory of jet structure, combined with jet mechanics, gas jet dynamics and impinging

152   jet mechanics et al. [22,23,24,25], the semi-analytical calculation approaches of jet flow was established.

153   **1) Initial Region of Free Jet**

154   Turbulence coefficient *a* is the characteristic coefficient of jet flow structure, and its value represents the

155   turbulence intensity at the outlet section. Turbulence coefficient *a* play a key role in determining the geometric

156   parameters of the jet, which is used to calculate the jet pole depth *d*, the initial jet length *c* and the inner boundary

157   contraction angle θ of the CO_2 jet.

158   The external boundary equation of jet is:

159    $$\frac{R}{r_0} = 3.4(\frac{as}{r_0} + 0.294).$$ (1)

160   Where *R* is the half width of the jet, r_0 is the nozzle outlet radius, *a* is the turbulence coefficient and *s* is the axis

161   length. In the high-pressure CO_2 jet, the turbulent coefficient *a* of the cylindrical nozzle is taken as 0.08, and the jet

162   diffusion angle α is generally 14.5°.

163   According to the external boundary equation, the jet pole depth *d*:

164    $$d = 0.294\frac{r_0}{a}.$$ (2)

165   The initial jet length *c*:

$$c = 0.67 \frac{r_0}{a}. \tag{3}$$

Derivation of nozzle outlet velocity based on one-dimensional constant entropy energy equation of gas:

$$u_0 = V = \sqrt{\frac{2k}{k-1} * RT_0[1 - (p_0/p)^{\frac{k-1}{k}}]}. \tag{4}$$

Where p_0 is the absolute pressure of the environment, p is the initial pressure of the jet at the nozzle outlet, $k = (i + 2)/i$ is the heat capacity ratio, i is the degree of freedom, $i = 3$ for single atom gas, 5 for diatomic gas and 6 for poly-atomic gas.

2) Development Region of Free Jet

In the development region of the free jet, the uniform velocity field of the jet core has disappeared. The jet gradually diffused from the axis to both ends, the CO_2 fluid gradually decreased, and the axial dynamic pressure of the jet gradually decreased.

The axial flow velocity calculation equation is:

$$\frac{u_m}{u_0} = \frac{0.96}{\frac{as}{r_0}+0.294} \tag{5}$$

The cross-section velocity distribution conforms to Gaussian probability distribution and has the following function relation:

$$\frac{u_y}{u_m} = \exp[-(\frac{y}{R})^2]. \tag{6}$$

The axial dynamic pressure distribution function is:

$$\frac{p_m}{p_0} = \begin{cases} 1 & (x \leq x_0), \\ \frac{x_0^2}{x^2} & (x \geq x_0). \end{cases} \tag{7}$$

Where $x_0 = c$ is the length of the initial jet.

The cross-section dynamic pressure distribution function is:

$$\frac{p}{p_m} = [1 - (\frac{y}{R})^{1.5}]^2. \tag{8}$$

3) Jet Impact Region

In the jet impact region, when the CO_2 jet impacts on the rock surface, the fluid dynamic pressure of jet parts gradually changes into static pressure. Consequently, the maximum impacting pressure exists at the center of the impact stagnation region, and large inclined pressure gradient forms in the region, as shown in Fig. 3:
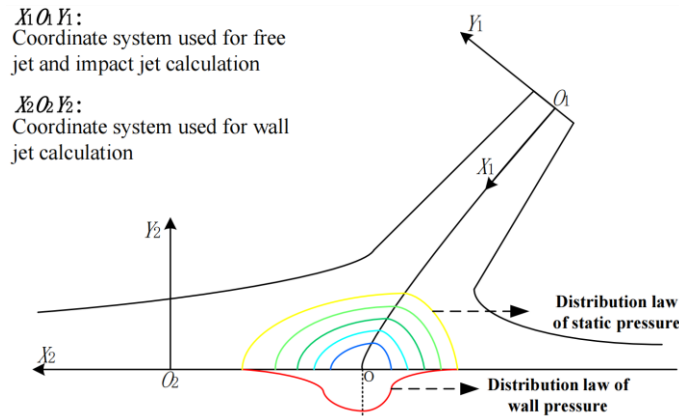
Fig. 3 The static pressure from the shock and the coordinates used for the calculation

The calculation formula of impact stagnation pressure p_s is:

$$p_s = 1.01306p_0 + 0.50824(p - p_0). \tag{9}$$

5

The distribution function of the axial static pressure p_m in jet impact region is:

$$\frac{p_m}{p_s} = \frac{3.2x_1}{H} - 2.2. \tag{10}$$

The distribution function of wall pressure p_w is:

$$\frac{p_w}{p_s} = \exp[-0.693(\frac{y_1}{R})^2]. \tag{11}$$

The front-to-back ratio of flux is:

$$\frac{q_2}{q_1} = \frac{1-\cos\varphi}{1+\cos\varphi} \tag{12}$$

4) Wall Jet Region

Due to the huge pressure difference between the jet impact region and the environment, the fluid in the jet impact region begins to diffuse outward along the wall, which produces the wall jet. Based on Glauret's wall jet velocity distribution theory [26], the radial wall jet velocity distribution was calculated.
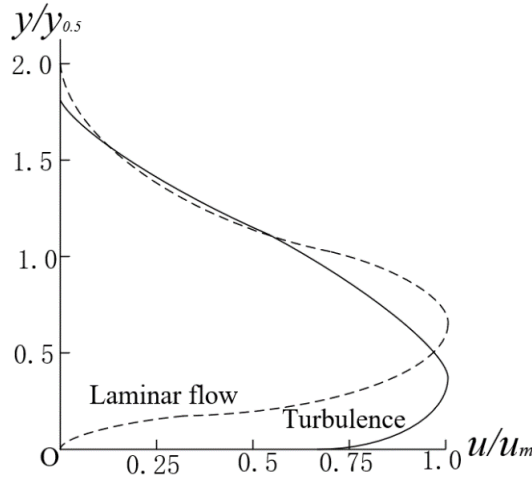
Fig. 4 wall jet velocity distribution

The wall jet is divided into two parts: the outer layer part with free jet characteristics and the inner layer part with obvious wall effect. The high-pressure CO_2 wall jet is assumed as a turbulent jet, so its boundary layer equation is:

$$u\frac{\partial u}{\partial x} + +v\frac{\partial u}{\partial y_2} = \frac{\partial}{\partial y}(\in \frac{\partial u}{\partial y}). \tag{13}$$

Where, $\in$ is the eddy viscosity, u and v denote the components of the mean velocity.

The equation of continuity is:

$$\frac{\partial x_2 u}{\partial x_2} + \frac{\partial x_2 v}{\partial y_2} = 0. \tag{14}$$

The boundary conditions are

$$u = v = 0 \ at \ y_2 = 0 \ , \quad u \to 0 \ as \ y_2 \to \infty \ . \tag{15}$$

The empirical formula of turbulent flow pipe τ_0 is introduced, in the form

$$\tau_0 = 0.0225\rho u^2(v/uy)^{0.25}. \tag{16}$$

Find the dimensionless similarity solution to the boundary layer equation, and consider the conditions for it, in which $u \propto x^a$, $\delta \propto x^b$. the formula requires that $\tau_0 \propto u^{7/4}u^{-1/4}$, and hence $\in \propto u^{3/4}\delta^{3/4} \propto x^{3(a+b)/4}$, And a, b need to satisfy $a + 5b = 4$.

Introduce dimensionless variables into the above equations

$$u = U\bar{u}, \quad v = U\bar{v}, \quad x = (v\bar{x})/U, \quad y = (v\bar{y})/U, \quad \psi = (v^2\bar{\psi})/U. \tag{17}$$

In accordance with the above results

6

$$\begin{cases} a. & \overline{\psi} = \bar{x}^{5-4b} f(\eta), \\ b. & \eta = \frac{5-4b}{\lambda} \bar{y} \bar{x}^{-b}, \\ c. & \in = A\lambda \bar{x}^{3-3b} f'^6 v. \end{cases} \qquad (18)$$

Where A and λ are constants.

Therefore, it can be obtained from the boundary layer equation (15) that

$$\frac{d}{d\eta}\left(Af'^6 f''\right) + ff'' + \alpha f'^2 = 0, \qquad (19)$$

Where $\alpha = (5b - 4)/(5 - 4b)$.

Combine Eq. (12) and Eq. (18), we can get

$$a = -9\alpha/(5 + 4\alpha) \ , \qquad b = (4 + 5\alpha)/(5 + 4\alpha) \quad . \qquad (20)$$

For the inner layer, the above formula can be used to calculate directly. For the outer layer, in place of Eq. (17c), as follows

$$\in = \lambda \bar{x}^{(3-3b)v}. \qquad (21)$$

For high-pressure CO_2 Impinge jet, the value of α is 1.3, the number of Reynolds is 5200 and other values are given by Glauret [26]. Referring to the above calculation method of velocity distribution, the calculation formulas of maximum velocity u_m and jet thickness δ of wall jet are obtained as follows

$$\frac{u_m b}{\sqrt{K}} = 1.32 \left(\frac{r}{b}\right)^{-1.1}, \qquad (22)$$

$$\frac{\delta}{b} = 0.098 \left(\frac{r}{b}\right)^{0.9}. \qquad (23)$$

Where K is mass flux, r is the distance from the impact stagnation point horizontally and b is the jet impact length.

Obviously, the flow field of the wall jet has obvious dependence on the initial characteristics of the impinging jet.

5) Impact Stagnation Region

The fluid in the wall jet region continues to flow forward until it impacts the surface of the PDC cutter. After that, the fluid cannot spread effectively in front of the cutter, because an acute angle region is produced between the PDC cutter and the rock surface, as is shown in Fig. 2. Therefore, the fluid in the acute angle region is defined as the fifth region in the jet flow field, named as impact stagnation region. Regrettably, there is no specific research on this region, so the flow structure and physical properties distribution in the impact stagnation region cannot be determined.

1.3 Physical Property Calculation

Compared with water, the CO_2 fluid has some unique physical properties, such as density, viscosity and compression coefficient, which dramatically varied close to the liquid-gas critical point (Pressure of 6.7131MPa, Temperature of 300K). Thus, the Virial state equation and the cubic state equation such as the PR state equation cannot accurately calculate the physical properties of CO_2, because these equations cannot converge near the critical point. In order to accurately calculate the physical properties of CO_2, the study applies the Span-Wagner state equation [27] to calculate properties.

The Span-Wagner state equation based on Helmholtz free energy was proposed by Span and Wagner in 1996 [27], which is specifically used to calculate the physical properties of CO_2. The error of density calculation is between 0.03% and 0.05%. It has a wide field of application that can accurately calculate the physical properties of CO_2 with temperature from 216.58 to 1100K and pressure from 0.52 to 800MPa.

Its dimensionless expression is

$$\frac{A(\rho,T)}{RT} = \Phi^o(\delta, \tau) + \Phi^r(\delta, \tau). \qquad (24)$$

261 Where $\delta = \rho/\rho_c$ is dimensionless density and $\tau = T_c/T$ is dimensionless temperature with $\rho_c = 467.6 kg/m^3$

262 and $T_c = 304.1282K$.

263 The ideal-gas part of the Helmholtz energy is

$$\Phi^o(\delta, \tau) = \ln(\delta) + a_1^o + a_2^o \tau + a_1^o \ln(\tau) + \sum_{i=4}^{8} a_i^o [1 - \exp(-\tau\theta_i^o)]. \tag{25}$$

265 The residual part of the Helmholtz energy is

$$\Phi^r(\delta, \tau) = \sum_{i=1}^{7} n_i \delta^{d_i} \tau^{t_i} + \sum_{i=8}^{34} n_i \delta^{d_i} \tau^{t_i} e^{-\delta c_i} + \sum_{i=35}^{39} n_i \delta^{d_i} \tau^{t_i} e^{-\alpha_i(\delta-\varepsilon_i)^2 - \beta_i(\tau-\gamma_i)^2} +$$

$$\sum_{i=40}^{42} n_i \triangle^{b_i} \delta e^{-C_i(\delta-1)^2 - D_i(\tau-1)^2}. \tag{26}$$

269 Where the parameters refer to nomenclature.

270 Based on the above numerical calculation equations, the thermodynamic properties and physical properties

271 distribution of high-pressure CO_2 jet in the model can be calculated. The calculation formulas of the physical

272 properties and thermodynamic properties based on the Span-Wagner state equation are listed below, respectively.

273 **Tab 1**. Calculation formulas of some thermodynamic properties based on Span-Wagner state equation

Property and common thermodynamic definition	Calculation formula
Pressure	$P(\delta, \tau) = (1 + \delta\Phi_\delta^r)\rho RT$
Enthalpy	$h(\delta, \tau) = (1 + \tau(\Phi_\tau^o + \Phi_\tau^r) + \delta\Phi_\delta^r)RT$
Entropy	$s(\delta, \tau) = (\tau(\Phi_\tau^o + \Phi_\tau^r) - \Phi^o - \Phi^r)R$
Internal energy	$u(\delta, \tau) = (\Phi_\tau^o + \Phi_\tau^r)\tau RT$
Isochoric heat capacity	$C_v(\delta, \tau) = -(\Phi_{\tau\tau}^o + \Phi_{\tau\tau}^r)\tau^2 R$
Isobaric heat capacity	$C_p(\delta, \tau) = (-\tau^2(\Phi_{\tau\tau}^o + \Phi_{\tau\tau}^r) + \dfrac{(1 + \delta\Phi_\delta^r - \delta\tau\Phi_{\delta\tau}^r)^2}{1 + 2\delta\Phi_\delta^r + \delta^2\Phi_{\delta\delta}^r})R$
Joule-Thomson coefficient	$\mu = \dfrac{-(\delta\Phi_\delta^r + \delta^2\Phi_{\delta\delta}^r + \delta\tau\Phi_{\delta\tau}^r)}{(1 + \delta\Phi_\delta^r - \delta\tau\Phi_{\delta\tau}^r)^2 - \tau^2(\Phi_{\tau\tau}^o + \Phi_{\tau\tau}^r)(1 + 2\delta\Phi_\delta^r + \delta^2\Phi_{\delta\delta}^r)R\rho}$

2 Calculation and Verification of CO₂ Jet

2.1 Calculation Method

276 The flow chart of theoretical calculation in this study is outlined in Fig. 5. The structure of the jet flow is

277 calculated by the semi-analytical approaches established in Sections 1.2 and 1.3. Then, based on the structural model

278 in Fig.2 and the semi-analytical approaches, the jet statures are divided into different regions. In every region, the

279 jet axis, the half width of the jet (ie the outer boundary of the jet), the initial velocity and the initial pressure are

280 established. In the manual grid model of the jet, the horizontal axis is set up every 0.5mm on the jet axis, and the

281 vertical axis is set up every 0.1mm depending on the horizontal direction. Every grid point generates by the

282 horizontal axis and vertical axis. Then, according to the cross-section pressure and velocity distribution function of

283 the jet, we can calculate the velocity or pressure value of each grid point. Thus, the velocity and pressure distribution

284 of the jet can be obtained by these gird points via the calculation of the above semi-analytical approaches.

285 However, these calculations methods cannot be used for the jet impact region and the wall jet region.

286 (1) For the jet impact region, we need to obtain the jet axis, outlet boundary, the front-to-back ratio of flux, and

287 the additional velocity generated in the jet impact region. During the jet impacting the wall, the jet axis line (X1),

288 see Fig.6, is always perpendicular to the wall. Therefore, a circular arc that tangents to the wall is regarded as the

289 actual axis line of the jet in the region. The front-to-back ratio of flux is calculated through Eq. (12). And the

290 additional velocity is calculated by the definition formula of dynamic pressure. The density in the definition formula

291 is calculated from the Span-Wagner state equation.

292 (2) For the wall jet region, a new coordinate system is established with the rock surface as the X_2 axis, see Fig.

293 3 and Fig. 6. Furthermore, the flow structure of the wall jet is completely different from that of the free wall jet.

294 Based on the wall jet theory of Gluent [26], the flow structure of the wall jet is determined by the maximum velocity

u_m, jet thickness δ and the cross-section velocity distribution function. Thus, the velocity and pressure distribution can be obtained from Eq. (19), Eq. (22) and Eq. (23).

For some properties cannot be directly captured or calculated. self-similar regular [26] approximate methods are used in the study. For example, the dynamic pressure in the wall jet region is obtained by similar velocity distribution in the region. Based on the above calculations, the dimensionless parameters of the Span-Wagner state equation can be obtained. Thus, through the calculation formulas of thermodynamic properties based on the Span-Wagner state equation, the most physical properties distribution of the jet can also be calculated, see Section 3 for details.
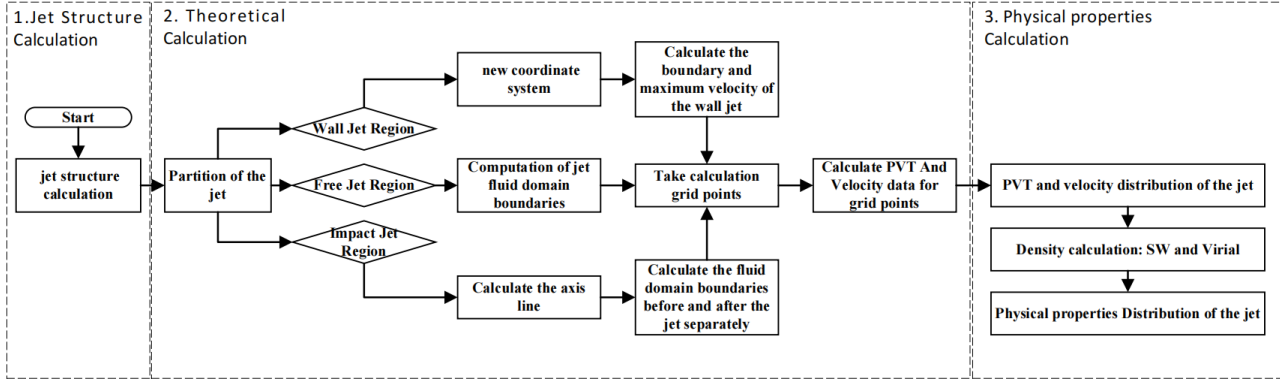
Fig. 5 Flow chart of theoretical calculation

2.2 Calculation Results of CO$_2$ Jet

Based on the semi-analytical approaches, the velocity and dynamic pressure distribution of high-pressure CO$_2$ jet was obtained, as shown in Fig. 6 to 8. Due to the sensitive influence of initial conditions, we will assume that the calculated case has a nozzle radius of 1mm, a jet distance of 15mm, a jet angle of 60°, a jet pressure of 20MPa, and a jet temperature of 300K. After the semi-analytical calculation, it shows that the initial jet velocity is 120.7m/s, the jet core length is 5.59mm, and the impact stagnation pressure is 10.215MPa.

Fig. 6 shows the dynamic pressure calculation results at different injection angles. It can be seen in the results that the CO$_2$ jet has obvious three parts such as jet core, shock stagnation region and wall jet. During the injection, a jet core is first generated at the nozzle outlet. In the jet core, the velocity and pressure of the fluid maintain the initial state of the jet. But on the boundary of the jet core, the fluid exchanges violently with the ambient fluid, and the pressure decays rapidly. After the fluid leaves the jet core, the pressure of the jet will attenuate, whether it is located at the axis or the periphery of the jet. And in the jet impact region, the dynamic pressure of the jet drops faster. Combined with the static pressure distribution in Fig.8, it can be seen that when the jet impacts on the rock surface and quickly converts from the dynamic pressure to static pressure, an impact stagnation region is produced in the impact region. Finally, the wall jet flows along the top rock surface because of the large pressure gradient. In addition, when the jet angle decreased from 75° to 45°, the axis line length was 14.89mm (75°), 14.58mm (60°) and 14.03mm (45°), respectively. These results indicated that the impact distance can reduce with the decrease of the jet angle.

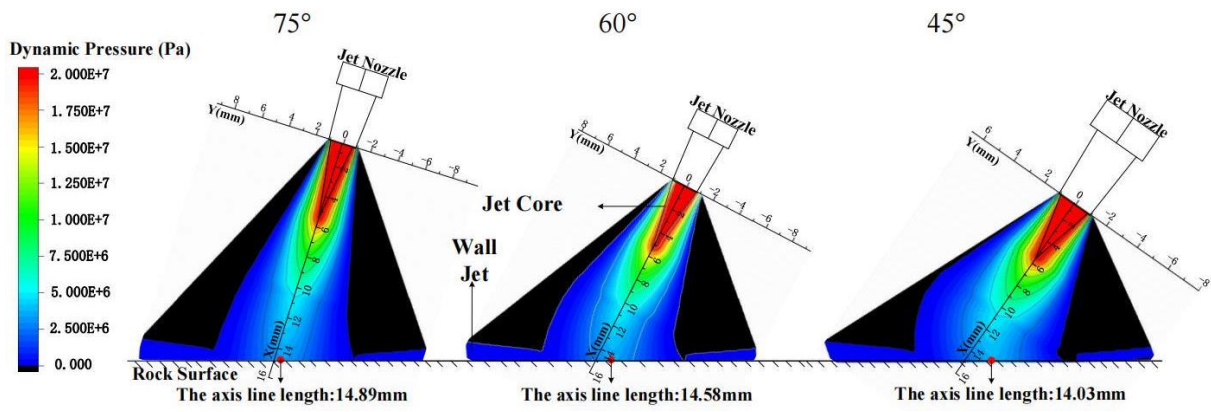Fig. 6. Dynamic pressure calculation results at different injection angles

Fig. 7 shows the velocity calculation results at different injection angles. The velocity distribution results are similar to the distribution of dynamic pressure. However, the half-value width of the velocity is slightly larger than that of the dynamic pressure, which indicates that the diffusion speed of the dynamic pressure is slightly larger than the velocity of the jet flow. The results are consistent with the previous studies [22,23]. When the jet angle decreased from 75° to 45°, the front-to-back ratio of flux were 1.702, 3.001 and 5.83, respectively. It shows that the decrease in jet angle was beneficial to composite rock breaking which can effectively enhance the debris-carrying and the cutter cooling. Therefore, during the composite working of the high-pressure CO_2 jet & PDC cutter, the decrease in the jet angle can effectively reduce the thermal wear of the cutter.
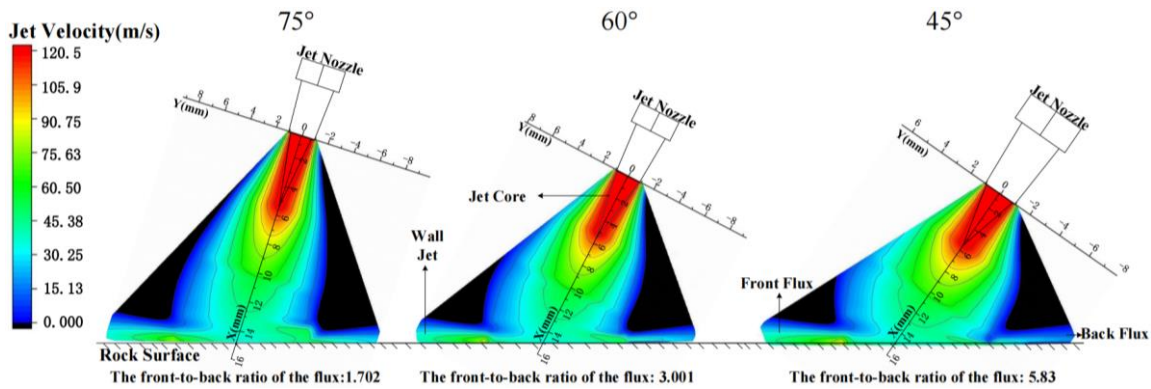
Fig. 7. Velocity calculation results at different injection angles

Fig. 8 shows the static pressure distribution at different injection angles. It includes the distribution of both static pressure and the impact pressure on the rock surface. In this case, it is assumed that the static pressure is the initial environment pressure, which is marked as blue color in Fig.8. In the jet impact region, the jet impact makes the velocity and dynamic pressure decrease and the static pressure increase. When the jet angle decreased from 75° to 45°, the maximum static pressure was 10.30MPa, 9.31MPa and 8.11MPa, respectively. The results show the impact force of the jet increase significantly with the increase in the jet angle. Thus, the reduction of the jet angle can improve rock-carrying and cutter cooling. Moreover, it can be seen that the greater the jet angle is, the greater the ratio of the half-value width Pw and the greater the ratio of the corresponding static pressure area are.
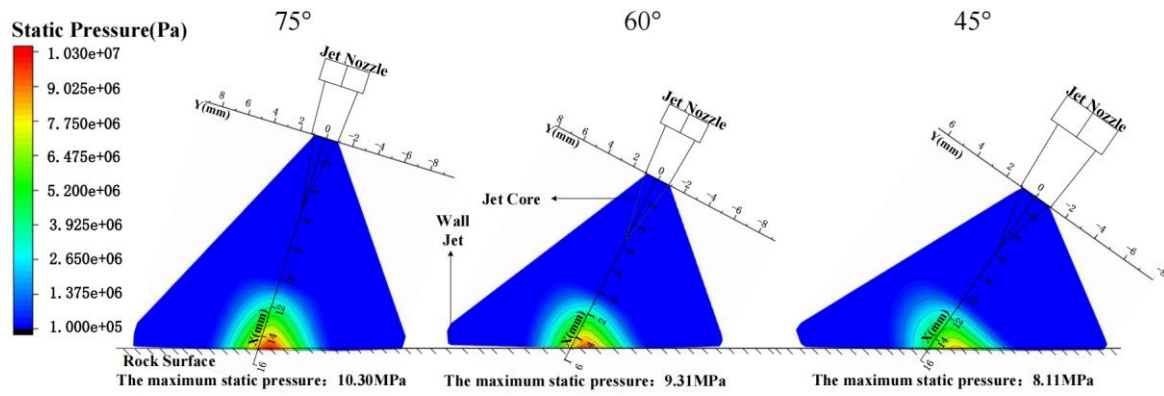
Fig. 8. Velocity calculation results at different injection angles

2.3 Comparison with Simulation and Experiment

Based on the physical model in Fig. 1, the rock-breaking numerical simulations and experiments of high-pressure CO_2 jet & PDC cutter were carried out [21]. Numerical simulation adopts a real-gas-model, which can simulate the change of CO_2 physical properties. Both the experiment and the numerical simulation use the same initial conditions as the above theoretical calculation. Then, our theoretical calculation is verified by using the numerical simulation and experimental results.
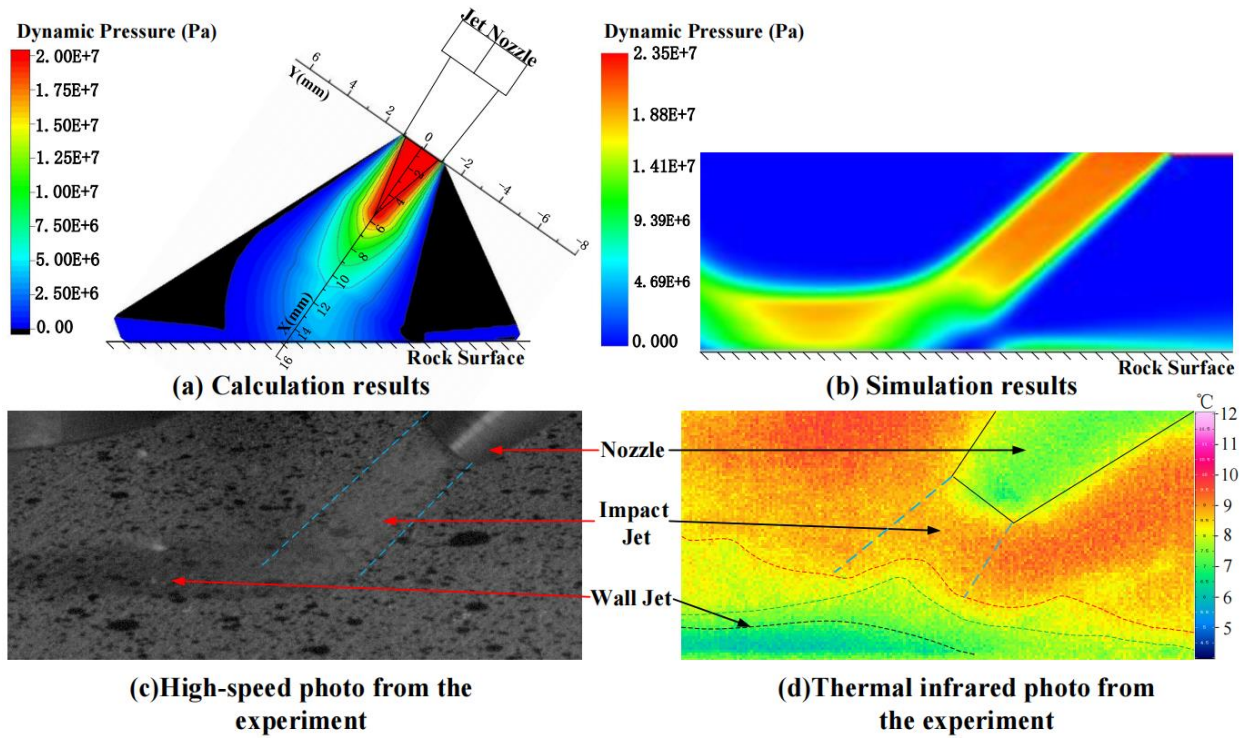
Fig. 9 Comparison of dynamic pressure distribution

As is shown in Fig. 9, the flow field of the CO_2 jet obtained by the semi-analytical approaches is compared with the experiments and the simulations. The initial dynamic pressure of the nozzle calculated by the semi-analytical approaches (Fig. 9(a)) is 10.3MPa, which is smaller than 15.7MPa obtained from the ANSYS fluent numerical simulation (Fig. 9(b)). Referring to the study of dynamic pressure in other documents [24,25], it can be seen that the pressure result calculated by semi-analytical approaches is closer to the experimental testing jet pressure. Fig. 9(c) and Fig. 9(d) are high-speed photography photos and thermal infrared photos of the high-pressure CO_2 jet, respectively. Compared with the experimental results, it can be seen that the flow field of theoretical calculation is similar to the experimental results and the numerical simulation results. The dynamic pressure of theoretical calculation has an obvious decline in the jet impact region, but the dynamic pressure of numerical simulation reduced slightly. It is noticed that the jet in Fig. 9(d) cannot be directly observed. The reasons are as

following: 1. The speed of the jet exceeds the frame rate of the thermal infrared camera, so the camera cannot capture temperature of the jet. 2. The jet in the experiment is a three-dimensional jet, so the camera can only capture the temperature at the periphery of the jet. According to the comparison, the verification indicates that the theoretical calculation could meet the engineering requirements for the composite rock-breaking model of high-pressure CO_2 jet & PDC cutter.

The static pressure distribution comparison between theoretical calculation and numerical simulation is shown in Fig. 10. It can be seen that the stagnation pressure obtained by the semi-analytical approaches is smaller than that by numerical simulation, its reasons is that the numerical simulation cannot simulate some complex influencing factors in real flow, such as friction and resistance. Therefore, its pressure is larger than the actual pressure. On the other hand, the range of the pressure area is also slightly different. Because of the semi-analytical approaches rely on the calculation results of the axis, so the static high-pressure region is inclined to the left. But overall, the calculation results of the two methods are extremely similar.

The physical properties distribution calculated by the semi-analytical approaches is similar to that of experiment and numerical simulation, which indicates that the calculation method of high-pressure CO_2 jet presented in the study is effective and reliable.
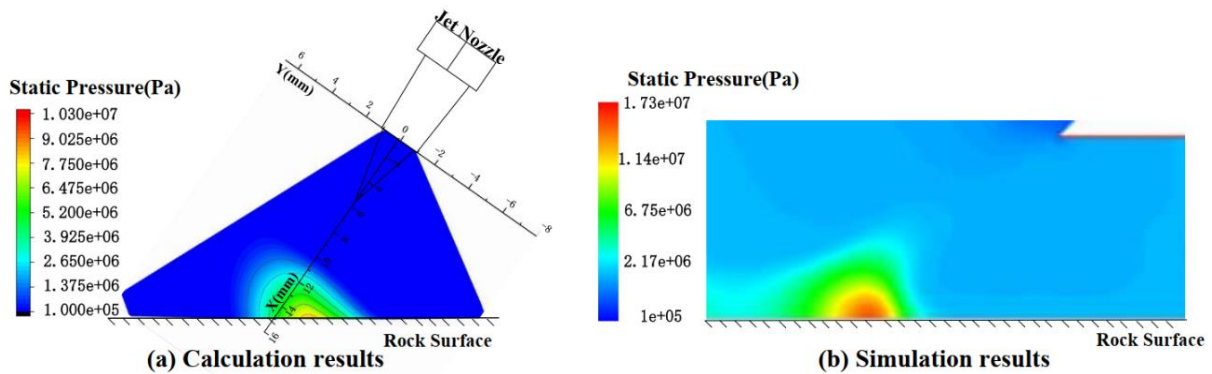
Fig. 10 Comparison of static pressure distribution

3 Calculation of Physical Properties based on Span-Wagner State Equation

Based on the PVT distribution in Section 2, the physical properties distribution of the high-pressure CO_2 jet could be obtained by the Span-Wagner state equation.

3.1 Method of Calculation

As shown in Fig.11, it is a pressure-density diagram of different state equations at a temperature of 300K. It can be seen from Fig.11 that the pressure calculated by the Span-Wagner equation is more realistic. Because CO_2 is in a phase transition state when the density is 268-679 Kg/m3, the density is a constant in this range. The Span Wagener state equation perfectly reproduces this process. The calculated data of the Virial state equation and the Redlich-Kwong (RK) state equation are relatively accurate when the pressure is low, but their calculation errors are very large when the pressure is higher than 5MPa. It can be seen that the Span-Wagner state equation is a better choice for calculating the physical properties of high-pressure CO_2, but the problem that it is not easy to converge at low temperature.
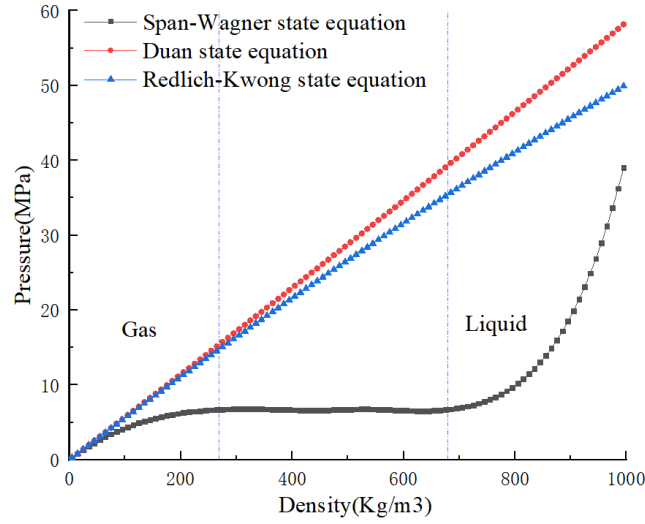
Fig 11 Density–Pressure variation diagram of different state equations

The Span-Wagner state equation is a multi-valued function and its density is an implicit equation. Therefore, in a large pressure range, the CO_2 density results calculated by the Span-Wagner state equation have a certain error. Because the iterative calculation of density cannot converge, as is shown in Fig. 12. When the temperature is lower than the critical temperature (304.1282K), the calculation results of the pressure appear violent fluctuations. The lower the temperature is, the more intense the pressure fluctuation is. The results show that when the temperature is lower than the critical temperature, the density results that are calculated by the Span-Wagner state equation will not converge.
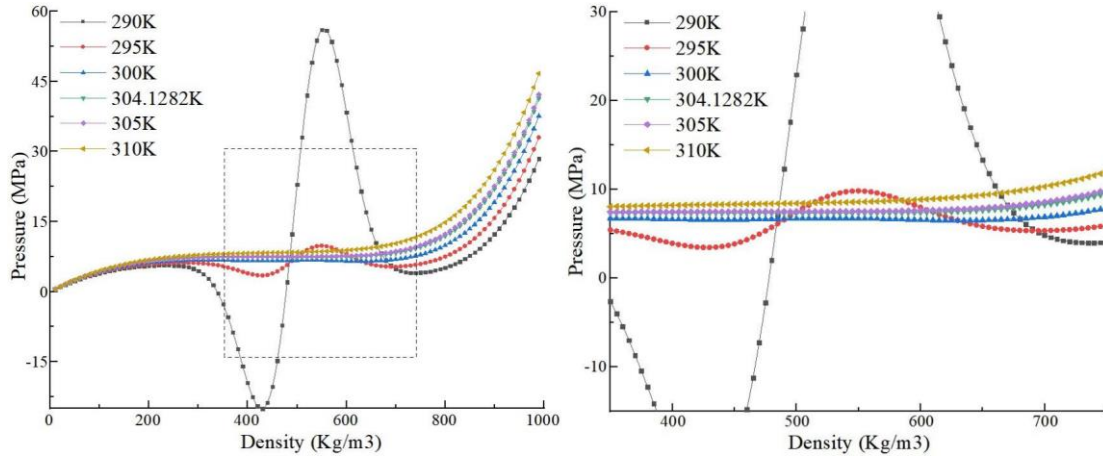
Fig. 12 Density–Pressure variation diagram of Span-Wagner state equation

To solve the above problems, the calculated density needs to be closer to the real value. Therefore, the density calculation method based on the combination of the Virial state equation and the Span-Wagner state equation was applied in the study. The Virial state equation adopted the equation proposed by Duan in 1992 [28], it has a higher accuracy for the density calculation of low-temperature and low-pressure CO_2, as follows:

$$Z = \frac{PV}{RT} = \frac{P_r V_r}{T_r} = 1 + \frac{B}{V_r} + \frac{C}{V_r^2} + \frac{D}{V_r^4} + \frac{E}{V_r^5} + \frac{F}{V_r^2}\left(\beta + \frac{\gamma}{V_r^2}\right)\exp(-\frac{\gamma}{V_r^2}) \tag{27}$$

Where B, C, D, E, F are functions of temperature, T_r is a dimensionless temperature based on critical temperature, V_r and P_r are similar to it.

Based on the dynamic pressure distribution in Fig. 6 and the initial temperature of the CO_2 jet, the density distribution of the CO_2 jet can be calculated. As is shown in Fig.13, when the calculated pressure is greater than the critical point (the gas-liquid critical point when the temperature is equal to 300K: the pressure is 6.7131MPa, the density is 679K/m3 (liquid), 268Kg/m3 (gas)), the CO_2 density in this region was calculated by the Span Wagner equation model, and the Duan model was used in other regions. In the study, the CO_2 jet is in a stable stage, so the

13

entire flow field was considered as a constant temperature field, and the study is also based on this hypothesis. To sum up, we obtain the density distribution and temperature distribution of high-pressure CO_2 jet, and the distribution of two dimensionless parameters δ and τ in the Span-Wagner state equation. Thus, the physical properties distribution of high-pressure CO_2 jets can be obtained.
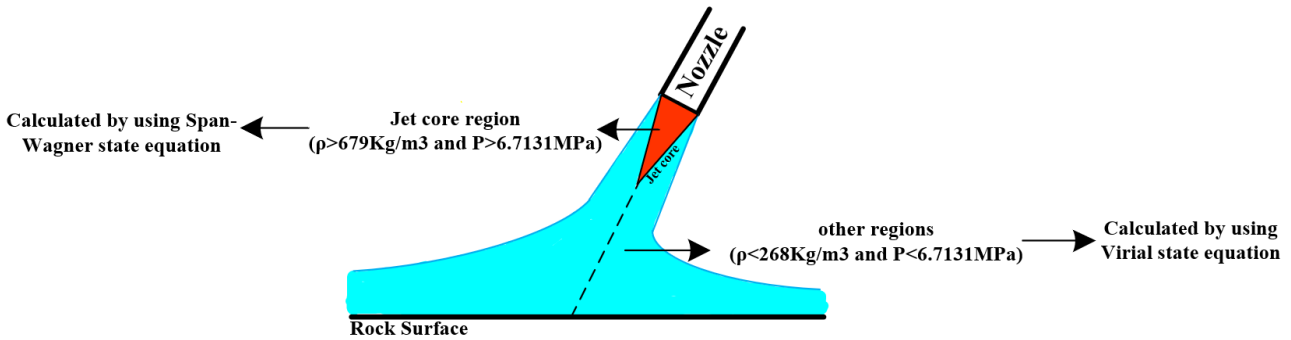
Fig. 13 Calculation Schematic

3.2 Results of Calculation

The density distribution of a high-pressure CO_2 jet at the nozzle angle of 45° is shown in Fig. 14. It can be seen that the distribution of density and dynamic pressure are similar. The CO_2 fluid is display as a high-density state in the initial region of the free jet, and the density reached 905.6 kg/m^3. In the development region and the boundary of the initial region of the free jet, the fluid spreads quickly to the surroundings, leading to the rapid decrease of density and pressure. In the jet impact region, the dynamic pressure of the fluid is converted into static pressure, so the density remains constant in the core region due to no energy loss. It is noticed that the density difference reached 800 Kg/m^3 between the initial region and the jet impact region. One of the reasons is that at a certain temperature, the relationship between pressure and density is likely an exponential function, as is shown in Fig. 11. After the large loss of the jet low in the development region, the maximum static pressure in the jet impact region is greatly lower than the initial jet pressure. The maximum impact pressure is only 0.52 times of the initial pressure. This is another reason for the density difference between the initial region and the jet impact region. The superposition of the two reasons presents the above results. In the wall jet region, the density of the CO_2 fluid is lower, which is consistent with the calculated results of pressure and velocity.
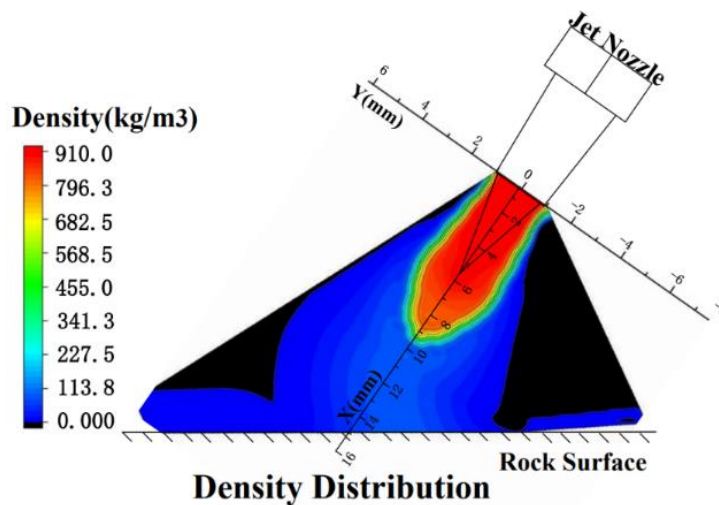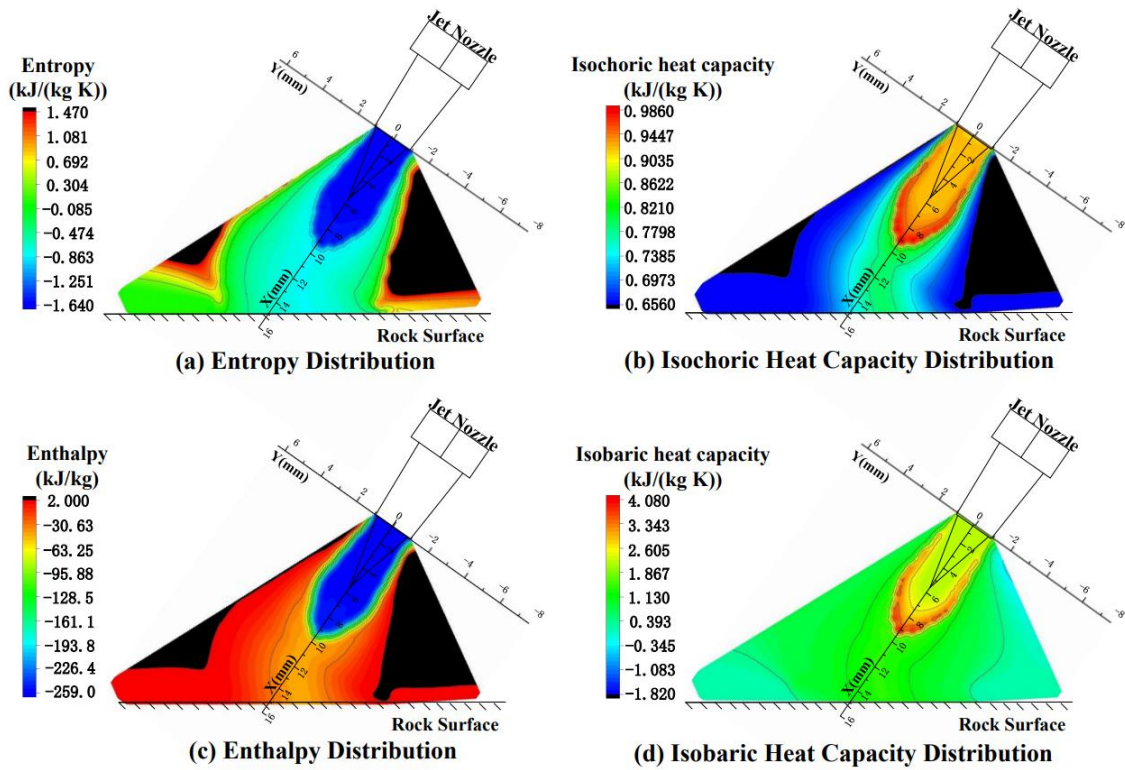

Fig. 14 Density distribution based on Span-Wagner equation

The distribution of some physical properties of the high-pressure CO_2 jet is shown in Fig. 14. It is noteworthy that both entropy (*S*) (Unit: Kj/ (Kg*K)) and enthalpy (*H*) (Unit: Kj/Kg) are state parameters. Therefore, to unify the calculation results, we define the *S* and *H* at the temperature of 298.15K and pressure of 0.101325MPa as 0 [27].

Fig. 15 (a) and (c) show the S and H distribution of the high-pressure CO_2 jet, respectively. In the initial region of the free jet, the S and H of CO_2 fluid are negative and the distribution is relatively uniform. It indicates that the fluid maintains a relatively stable state in the jet core. At the other region of the jet, the S and H of the fluid increase sharply. The value of S and H increased from -1.64 to -0.474, -259 to -30.63, respectively. The changes value of H reached 230. It shows that the jet and the ambient fluid undergo intense mixing and heat exchange in this region, and the CO_2 fluid absorbs a lot of heat [29]. Due to the pressure difference between the nozzle inlet and ambient pressure, the jet rapidly spreads around, and forms the jet core after ejection. This process is accompanied by a dramatic increment in S and H. At the boundary of the jet, the S and H of CO_2 fluid sharply increased to 1.470 and 2.03, respectively. This increasing trend indicates that the CO_2 jet is sufficiently and vigorously mixed with the ambient fluid. In addition, the H is negative in most regions, revealing that there is intense heat-absorption of high-pressure CO_2 jet with ambient fluid. During the composite rock breaking of the high-pressure CO_2 jet & PDC cutter cutting, CO_2 fluid can effectively absorb the heat of the debris and reduce the thermal wear of the PDC cutter.

Fig. 15 (b) and (d) show the isochoric heat capacity (Cv) and isobaric heat capacity (Cp) distribution of the high-pressure CO_2 jet, respectively. It can be seen that at the outer edge of the jet core and the development region of the free jet, both Cv and Cp were highest and reached 0.986 and 4.08, respectively. The results show that the heat-absorption ability of the jet fluid is the strongest at the region than other regions. Therefore, combined with the entropy change and enthalpy change of the jet fluid, it is noticed that the high-pressure CO_2 jet has an intense cooling [21], and this ability is strongest in the outer edge of the jet core and the development region of the free jet.

Fig. 15 Physical properties distribution based on Span-Wagner equation

4 Analysis of Jet Physical Properties Distribution Feature

The influencing factors of high-pressure CO_2 jet are shown in Tab 2. Where the parameter in bold is the parameters of the based group. Comprehensively study of the high-pressure CO_2 jet physical properties distribution law is carried out.

Tab 2 Influencing factor of the calculation (the parameters format which is bold means the based group)

Influencing factors	Control group
Jet pressure	10MPa, **20MPa**, 30MPa, 40MPa

Jet distance	10cm, **15cm,** 20cm, 25cm
Nozzle diameter	1cm, **2cm**, 3cm, 4cm
Jet angle	45°,**60°**,75°

4.1 Jet Pressure

Fig. 16 shows the distribution of physical properties on the jet axis at different jet pressure. it can be seen that when the initial pressure was 40MPa, the minimum density of the jet was higher and reached 824.98 Kg/m^3. As the initial pressure rose to 30MPa, the minimum density dropped to 778.46 Kg/m^3, and the maximum value of S and H increased from -1.56, -248.45 to -1.53, -241.14, respectively. Although the pressure was reduced by 10MPa, the change in physical properties was not drastic. However, when the jet pressures were 20MPa and 10MPa, respectively, the jet density, S and H have a cliff-like variation in the development region of the free jet. When the initial pressure was 20MPa, the minimum density of the jet was 97.73 Kg/m^3. And when the initial decreased to 10MPa, the minimum density dropped to only 48.37 Kg/m^3, the maximum value of H reached -22.856. The results indicate that a specific value exists between 20MPa and 30MPa of initial pressure, and the physical properties of the jet show distinct properties on both sides of this value. It can be seen from Fig. 16 (b) that when the initial pressures were 20MPa and 10MPa, respectively, the dynamic pressure on the boundary between the free jet and the impact jet was below the critical point (6.7131MPa). It indicates that the jet fluid has a phase transition from the liquid state to the gas state before this boundary. It is the primary cause of the drastic change in physical properties. When the initial pressures were 30MPa and 40MPa, the dynamic pressure on the boundary was higher than the critical point. So, there was no obvious phase transition, and the physical properties changes are relatively smooth. In the jet impact region, the dynamic pressure was converted into static pressure, the total pressure remains constant, resulting in no energy loss on the axis. Therefore, the physical properties such as density, S and H do not change.

The results show that the CO_2 jet pressure has a great influence on the change of the physical properties, especially at critical pressure (6.7131MPa) of the phase transition. When the jet pressure is lower than the critical pressure, the fluid will undergo a liquid-gas phase transition, resulting in a dramatic change in the physical properties. Therefore, the increase in initial pressure can effectively increase the impact force and the cooling of the jet.
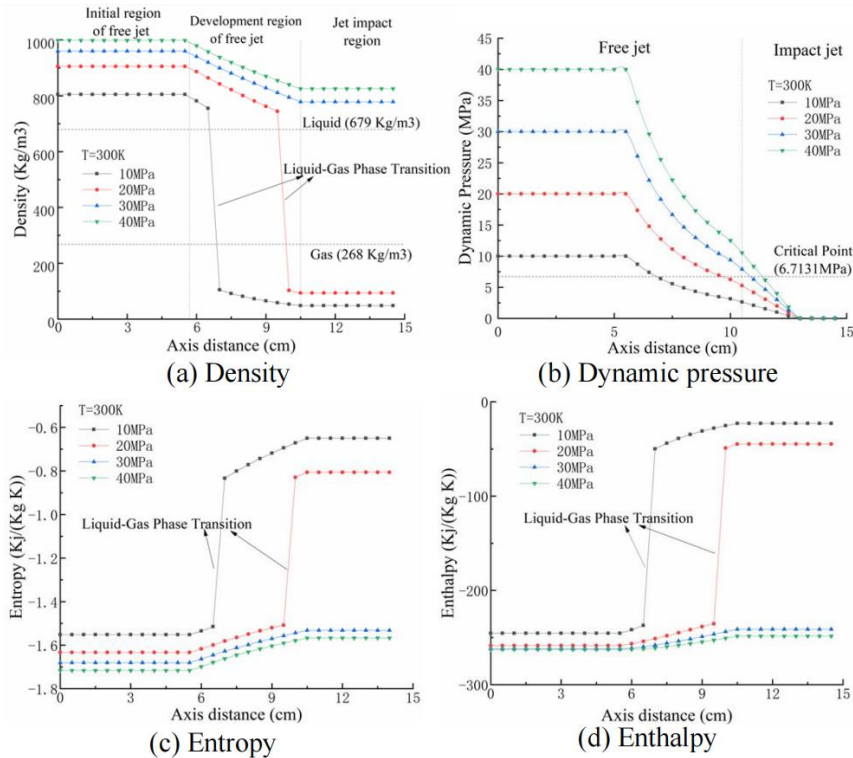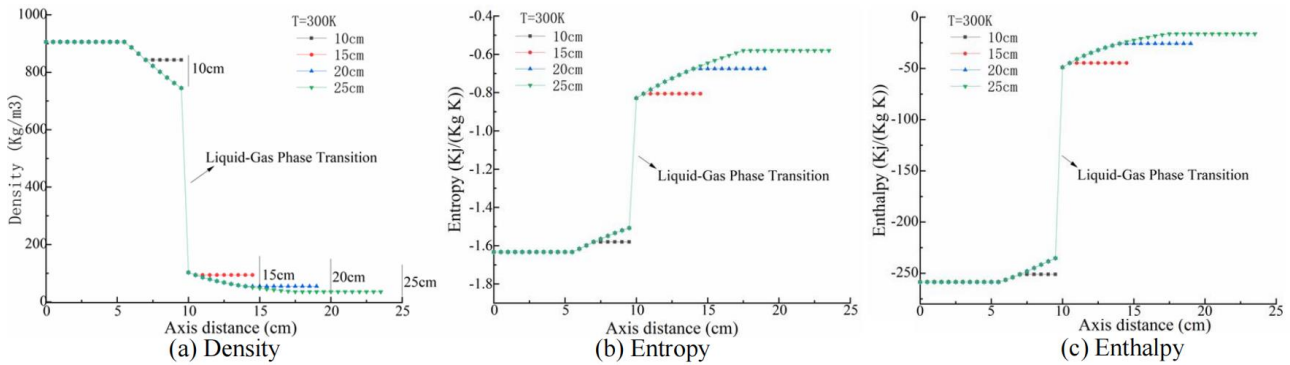

Fig. 16 Distribution of physical properties on jet axis at different jet pressures

4.2 Jet Distance

Fig. 17 shows the distribution of physical properties on the jet axis at a different jet distance. It can be seen that with the increase in the jet distance varied from 10cm to 25cm, the CO_2 jet minimum density gradually decreases from 842.79 Kg/m^3 to 35.15 Kg/m^3, and the maximum value of S and H gradually increases from -1.58, -251.14 to -0.58, -16.287, respectively. Similar to the effect of pressure, there also is a phase transition critical distance of jet distance between 10cm and 15cm. When the jet distance is greater than this distance, the phase transition occurred in CO_2 jet fluid. When the jet distance further dropped from 20cm to 25cm, the density decreased from 54.19 Kg/m^3 to 35.15 Kg/m^3. It shows that the density reduction is also own to the natural diffusion in the development region of the free jet. With the increase in jet distance, the energy loss increased gradually.

Furthermore, the actual distance of the jet in Fig. 17 is smaller than the theoretical jet distance. Due to the gravity and stagnation region, the axis of the jet is an arc segment offset downward, as shown in Fig. 2. Therefore, the actual jet distance is smaller than the theoretical jet distance. The results show that when other parameters are consistent, the variation of jet distance influences the overall physical property distribution of the jet. For the application of CO_2 jet, a shorter jet distance can bring greater impact force and cooling ability. And at the same time, a shorter jet distance can ensure that the jet impact is more accurate.

Fig. 17 Distribution of physical properties on jet axis at different jet distance

4.3 Nozzle Diameter

Fig. 18 shows the distribution of physical properties on the jet axis at different nozzle diameters. It can be seen that with the increase in the nozzle diameter, the variation of the physical properties curve gradually becomes smooth. When the nozzle diameter is greater than 3 cm, the CO_2 jet would not experience the phase transition, and the fluid density remains a high value. Overall, the nozzle diameter increased from 1cm to 4cm, the length of the jet core (ie the Eq. (3)) gradually increases, which are 2.79 cm, 5.59 cm, 8.38 cm, 11.18 cm, respectively. Under the same jet distance, the jet core length increased with an increase in nozzle diameter. Thus, the CO_2 jets with shorter core lengths decay earlier than the jets with longer core lengths. When the density or pressure decreases to the critical point value, the CO_2 jet would cross the liquid-gas phase position, resulting in a sharp change in the physical properties, as is shown in Fig. 18. Therefore, the larger nozzle diameter makes the impact force of jet stronger.
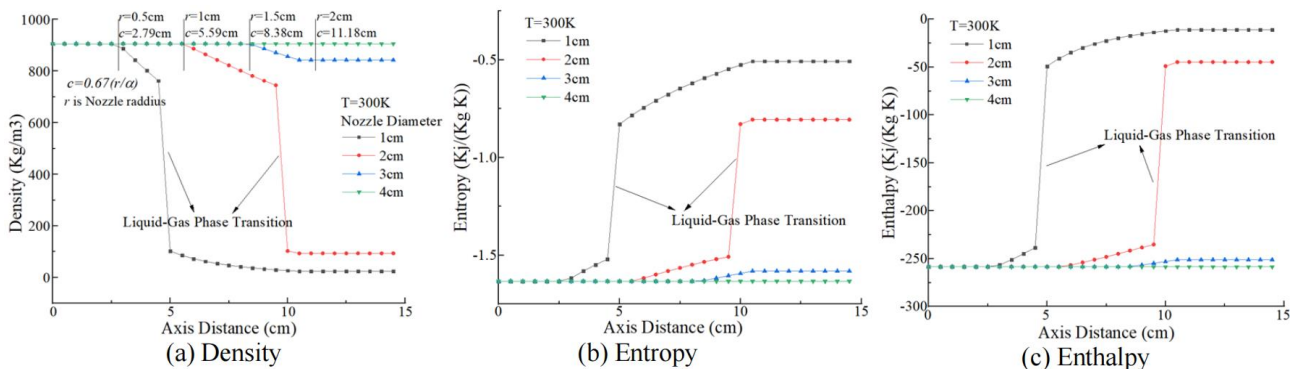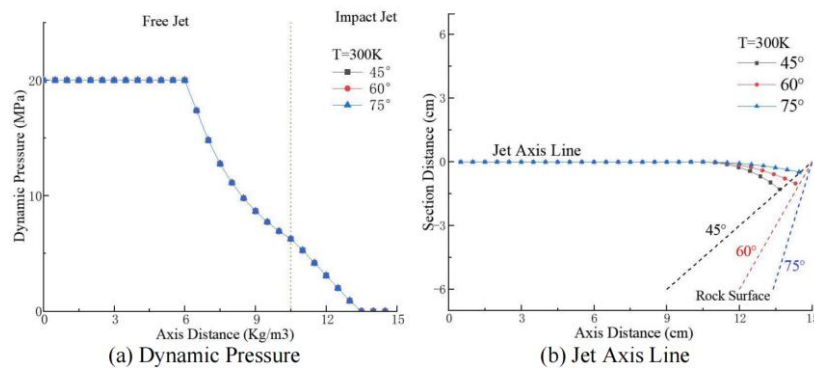

Fig. 18 Distribution of physical properties on jet axis at different nozzle diameter

17

4.4 Jet Angle

Fig. 19 shows the effect of the jet on the jet axis at a different jet angle. At first, it can be seen from Fig. 19 (a) that the jet angle has no obvious effect on the physical property distribution. However, it can be seen from Fig. 19 (b) that the arc section of the jet axis gradually changes with the increase in jet angle. When the jet angle increased from 45° to 75°, the radians were 0.785, 1.047 and 1.308, respectively. Thus, the increases in the jet angle can increase the distance between the nozzle and impact stagnation point. During the jet impacting, the axis of the jet is always perpendicular to the wall, and the ratio of the front and rear flow of the jet is inversely proportional to the jet angle [22,23]. Therefore, the jet angle has a great influence on the flow field structure of the jet, but the distribution of physical properties on the jet axis is not affected, as shown in Fig. 6, Fig. 7 and Fig. 8.

In summary, the jet pressure, the ratio of nozzle diameter and jet length is a consideration for rock-breaking of high-pressure CO_2 jet & PDC cutter. If a stronger impact capability is required for rock breaking, it is necessary to increase the density of the CO_2 jet. That means we need to increase the jet pressure, increase the nozzle diameter, and reduce the jet distance. Then, the CO_2 jet cannot easily produce a phase transition within a limited distance. it is noticed that the jet angle would affect the arc section of the jet axis, finally does an important role in the flow structure of the CO_2 jet. With the decreases in the jet angle, the structure of the jet becomes a more uneven distribution. Therefore, a smaller jet angle is more conducive to the divergence of the fluid and is not conducive to the impact of the fluid.

Fig. 19 Distribution of physical properties on jet axis at different jet angle

5 Conclusion

Based on the Span-Wagner state equation and CO_2 jet theory, a semi-analytical approach of high-pressure CO_2 jet flow field was established for composite rock breaking. Through semi-analytical calculations and physical properties calculations with the high-pressure CO_2 jet, the physical properties distribution law was explored considering the factors of jet pressure, jet distance, nozzle diameter and jet angle. The conclusions are drawn as follows:

1) The physical properties distribution calculated by the semi-analytical approaches is similar to that of experiment and numerical simulation, which indicates that the calculation method of high-pressure CO_2 jet presented in the study is effective and reliable.

2) At the temperature of 300K and the initial pressure of 20MPa, the density difference can reach to 800 Kg/m^3 between the initial region and the jet impact region. Under the influence of the liquid-gas phase transition, the enthalpy of the jet changes drastically over 230 Kj/ (Kg*K) in the flow field. It indicates that the jet fluid experiences intense heat exchange.

3) When the jet distance is 15cm and the nozzle diameter is 1cm, a critical point exists between 20MPa and 30MPa of initial pressure, and the physical properties of the jet show totally different properties on both sides of this point. Similarly, the critical point could be easily obtained when the jet distance varied from 10cm to 15cm of jet distance, nozzle diameter varied from 2cm to 3cm.

4) At the temperature of 300K, the rise in initial pressure can effectively increase the impact force and the cooling ability of the jet. The rise in the ratio of nozzle diameter and jet length can increase the proportion of the jet core lengths in the jet on the axis, which can enhance the impact force of the jet. The increase in the jet angle can increase the impact force of the fluid, but it is not conducive to fluid diffusion.

5) To sum up, in the design of downhole tools based on CO_2 jet, the ratio of jet nozzle diameter and jet distance should be considered first to ensure that the jet can achieve ideal working efficiency when it hits the rock. Secondly, jet angle is also a problem that must be considered in the design. Choosing a suitable angle can make the debris-carrying capacity and impact capacity to be more efficient and balance.

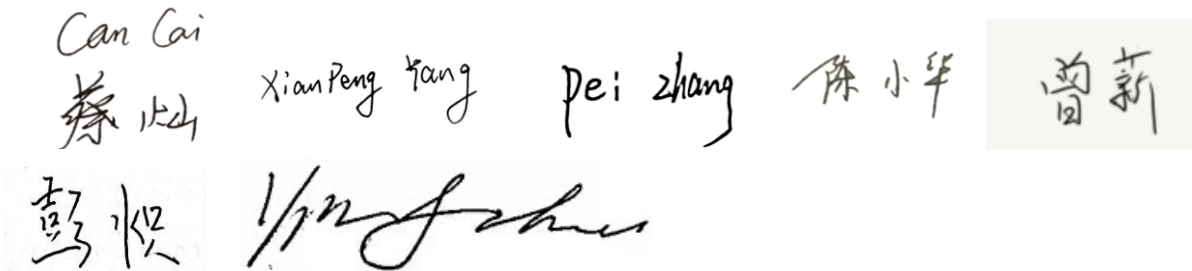## Compliance with Ethical Standards

1) Conflict of Interest

The authors declare that they have no conflict of interest.

The authors declare that they have no known competing financial interests, non-financial interests, or personal relationships that could have appeared to influence the work reported in this paper.

Signature:

3) Ethical approval

This article does not contain any studies with human participants or animals performed by any of the authors.

4) Informed consent

Informed consent was obtained from all individual participants included in the study.

Author contributions

All authors contributed to the study conception and design. Material preparation, data collection and analysis were performed by Xian-Peng Yang, Can Cai and Pei Zhang. The first draft of the manuscript was written by Xian-Peng Yang, Can Cai. Yingfang Zhou have gave valuable comments for the submitted manuscript. All authors commented on previous versions of the manuscript. All authors read and approved the final manuscript.

Reference

[1] Shen, Z.H., Wang, H.Z., Li, G.S., 2010. Feasibility analysis of coiled tubing drilling with supercritical carbon dioxide. Petrol Explor Dev+. 37(6), 743-747. https://doi.org/10.1016/S1876-3804(11)60008-6

[2] Kolle, J.J., Marvin, M., 2000. Jet-assisted coiled tubing drilling with supercritical carbon dioxide. Proceedings of ETCE/OMAE 2000 Joint Energy

Conference, New Orleans, USA.

[3] Du, Y.K., Wang, R.H., Ni, H.J., et al., 2012. Determination of rock-breaking performance of high-pressure supercritical carbon dioxide jet. J Hydrodyn. 24(4), 554-560. https://doi.org/10.1016/S1001-6058(11)60277-1

[4] He, Z.G., Li, G.S., Tian, S.C., et al., 2016. SEM analysis on rock failure mechansim by supercritical CO_2 jet impingement. J Petrol Sci Eng. 146, 111-120. https://doi.org/10.1016/j.petrol.2016.04.023

[5] Huang, M., Kang, Y., Wang, X.C., et al., 2018. Experimental investigation on the rock erosion characteristics of a self-excited oscillation pulsed supercritical CO_2 jet. Appl Therm Eng. 139, 445-455. https://doi.org/10.1016/j.applthermaleng.2018.05.014

[6] Li, M.K., Ni, H.J., Cao, Y.G., et al., 2020. Flow energy transformation and dissipation mechanisms of carbon dioxide, nitrogen, and water jets. J Nat Gas Sci Eng. 84, 103650. https://doi.org/10.1016/j.jngse.2020.103650

[7] Kim, D.S., Lee, J., 2016. Experimental investigation of CO_2 dry-ice assisted jet impingement cooling. Appl Therm Eng. 107(2), 927-935. https://doi.org/10.1016/j.applthermaleng.2016.07.054

[8] Wang, T., Zhou, W. B., Chen, J. H., et al., 2014. Simulation of hydraulic fracturing using particle flow method and application in a coal mine. Int J Coal Geol, 121, 1-13. https://doi.org/10.1016/j.coal.2013.10.012

[9] Wang, T., Hu, W. R., Elsworth, D., et al., 2017. The effect of natural fractures on hydraulic fracturing propagation in coal seams. J Petrol Sci Eng, 150, 180-190. https://doi.org/10.1016/j.petrol.2016.12.009

[10] Cai, C., Gao, C., Wang, H.Z., et al., 2021. Flow field and cuttings removing enhancement under composite rock-breaking of high-pressure CO_2 jetting & PDC tooth. Natural Gas Industry. 41(10), 1-10.

[11] Cai, C., Xie, S., Liu, Q.R., et al., 2020. The Flow Characteristics of Supercritical Carbon Dioxide (SC-CO_2) Jet Fracturing in Limited Perforation Scenarios. Energies. 13(10), 1-19. https://doi.org/10.3390/en13102627

[12] Chen, H., Hu, Y., Kang, Y., et al., 2021. Advantages of supercritical CO_2 compound fracturing in shale on fracture geometry, complexity and width. J Nat Gas Sci Eng. 93, 104033. https://doi.org/10.1016/j.jngse.2021.104033

[13] Wang, H.Z., Li, G.S., Shen, Z.H., et al., 2015. Experiment on rock breaking with supercritical carbon dioxide jet. J Nat Gas Sci Eng. 127, 305-310. https://doi.org/10.101-6/j.petrol.2015.01.00

[14] Huang, M., Kang, Y., Wang, X.C., et al., 2018. Analysis of the flow characteristics of the high-pressure supercritical carbon dioxide jet. J Hydrodyn. 31(2), 389-399. https://doi.org/10.1007/s42241-018-0165-8

[15] Li, M.K., Wang, G., Cheng, W.M., et al., 2021. Heat-fluid-solid coupling mechanism of supercritical carbon dioxide jet in rock-breaking. Petrol Explor Dev+. 48(6), 1450-1461. https://doi.org/10.1016/S1876-3804(21)60301-4

[16] Miller, R.G., 1994. Fundamental study of carbon dioxide blasting: An experimental and numerical analysis of surface cleaning by a particle-laden turbulent jet. Michigan Technological University.

[17] Khalil, I.G., 2003. Free-jet expansion of supercritical carbon dioxide. University of California, San Diego.

[18] Cheng, Y.X., Li, G.S., Shen, Z.H., et al., 2014. Impact pressure and parametric sensitivity analysis of supercritical $C0_2$ jet. Acta Petrolei Sinica. 35(4), 765-770. https://doi.org/10.7623/syxb201404020

[19] Zhou, Z., Lu, Y.Y., Tang, J.R., et al., 2017. Numerical simulation of supercritical carbon dioxide jet at well bottom. Appl Therm Eng, 121(3), 210-217. https://doi.org/j.applthermaleng.2017.04.06

[20] Huang, F., Hu, B., 2018. Macro/micro-behavior of shale rock under the dynamic impingement of a high-pressure supercritical carbon dioxide jet. RSC Advances. 8(66),38065-38074. https://doi.org/10.1039/c8ra07480a

[21] Cai, C., Yang, X.P., Gao, C., et al., 2022. Intense cooling during composite rock-breaking of high-pressure CO_2 jet- Polycrystalline diamond cutter. SPE J. https://doi.org/10.2118/209603-PA

[22] Zhao, C.Q., Jiang, Y., 1998. Gas Jet Dynamics. Beijing, Beijing Institute of Technology Press.

[23] Dong, Z.Y., 2005. Jet mechanics. Beijing, science Press.

[24] Hu, Y., Kang, Y., Wang, X.C., et al., 2016. Experimental and theoretical analysis of a supercritical carbon dioxide jet on wellbore temperature and pressure. J Nat Gas Sci Eng. 36(A),108-116. https://doi.org/10.1016/j.jngse.2016.10.014

[25] Bai, X., 2019. Research on Mechanism and Application of Liquid Carbon Dioxide Phase Change Jet Fracturing Coal Seam to Increase Gas Permeability. Chongqing, Chongqing University.

[26] Glauert, M.B., 1956. The wall jet. J Fluid Mech. 1(6), 625-643. https://doi.org/10.1017/S002211205600041X

[27] Span, R., Wagner, W., 1996. A new state equation for carbon dioxide covering the fluid region from the triple point temperature to 1100 K at

639   pressures up to 800MPa. J Phys Chem Ref Data. 25(6),1509-1596. https://doi.org/10.1063/1.555991

640   [28] Duan, Z.H., Miller, N., Weare, J.H., 1992. An equation of state for the CH_4-CO_2-H_2O system: I. Pure systems from 0 to 1000°C and 0 to 8000 bar.

641   Geochrmica ef Cosmochimrca Acra. Vol. 56: 2605-2617.

642   [29] Roebuck, J.R., Murrell, T.A., Miller, E.E., 2002. The joule-thomson effect in carbon dioxide. J Am Chem Soc 64 (2): 400-411.

643   https://doi.org/101021/ja01254a048